Seismic noise tomography in the Chile ridge subduction region

A. Gallego,[1] R. M. Russo,[1] D. Comte,[2] V. I. Mocanu,[3] R. E. Murdie,[4] and J. C. Vandecar[5]

[1]*Department of Geological Sciences, P.O. Box* 112120, 241 *Williamson Hall, University of Florida, Gainesville, FL* 32611, *USA. E-mail: agallego@ufl.edu*
[2]*Department de Geofisica, Blanco Encalada* 2002, *Universidad de Chile, Santiago, Chile*
[3]*Department of Geophysics, Bucharest University,* 6 *Traian Vuia Street,* RO-7139 *Bucharest* 1, *Romania*
[4]*Gold Fields Australia, St Ives Gold Mine, P.O. Box* 359, *Kambalda, WA* 6442, *Australia*
[5]*DTM, Carnegie Inst. of Washington,* 2541 *Broad Branch Road, Washington DC* 20015, *USA*

SUMMARY

We used cross-correlation of ambient seismic noise recorded in the Chile Triple Junction (CTJ) region to estimate interstation surface wave time-domain Green's functions, and then inverted traveltimes to obtain crustal surface wave velocity models. Interstation distances within the Chile Ridge Subduction Project (CRSP) temporary seismic network ranged from 40 to ∼100 km. We selected 365 d, and cross-correlated and stacked 24 hr of vertical component data at 38 stations pairs, resulting in nominally 703 traveltimes along assumed-straight interstation paths. Velocities in 2-D cells of 30 km × 30 km were calculated using a linear least-squares inversion of the Rayleigh wave group velocity traveltimes. Furthermore we performed a Rayleigh wave group velocity dispersion analysis to estimate the sensitivity of different period waves at depth and to calculate a 3-D shear velocity model of the Patagonian crust. The process was applied to cross correlation pairs determined in two period bands, 5–10 s, corresponding to shallow crustal velocities down to approximately 10 km depth, and 10–20 s, for velocities down to around 20 km. Our results show that cell velocities correlate well with known geological features. We find high-crustal velocities where the Patagonian Batholith outcrops or is likely present at depth, and low velocities correlate with the active volcanic arc of the Southern Volcanic Zone and the subducted Chile ridge in Taitao peninsula, where thermal activity of hot springs is present. High velocities in the mountainous portions of the southeastern study area appear to correlate with outcropping older metamorphic units. Low velocity in the east correlate with sequences of volcaniclastic deposits.

Key words: Surface waves and free oscillations; Wave scattering and diffraction; Wave propagation; Continental margins: convergent; Crustal structure; Rheology: crust and lithosphere.

GJI Seismology

1 INTRODUCTION

1.1 Background: Ambient noise tomography

Studies of scattered sound waves in inhomogeneous media (Lobkis & Weaver 2001; Larose *et al.* 2004) have found recent application in seismology in a new technique called ambient noise tomography, whereby it is possible to invert for seismic velocities of the lower and upper crust without having recourse to either passive or active seismic sources (Campillo & Paul 2003; Shapiro & Campillo 2004; Snieder 2004; Shapiro *et al.* 2005; Gerstoft *et al.* 2006; Bensen *et al.* 2007; Lin *et al.* 2007). Long-period seismic noise from sources such as ocean waves generates long-period surface waves that travel in the Earth's crust. At long distances, attenuation due to scattering eventually reduces the coherence of the signal and original direction of propagation. However, empirically, and theoretically, it is possible to enhance the signal coherence and obtain a Green's function of the surface wave propagation by cross-correlating long time-series of interseismic noise seismograms between stations pairs (Shapiro & Campillo 2004; Snieder 2004).

In the ideal situation where seismic noise sources or scatterers are uniformly distributed between two stations, the cross-correlated noise signal will be a symmetric function with respect to the arrival time. However, when the noise source is concentrated along one azimuth, the cross-correlation will be one sided (e.g. Gerstoft *et al.* 2006). Because longer period scattered waves correspond to propagation at deeper levels, different frequency bands can be used to resolve velocity models at specific depth ranges (Gerstoft *et al.* 2006; Bensen *et al.* 2007; Lin *et al.* 2007).

1.2 Subduction of the Chile ridge

We applied the ambient noise Green's function technique to data collected during a temporary seismic deployment in the Chile Triple Junction (CTJ) of northern Patagonia (Fig. 1), a remote region of very difficult access that has been poorly studied. The current
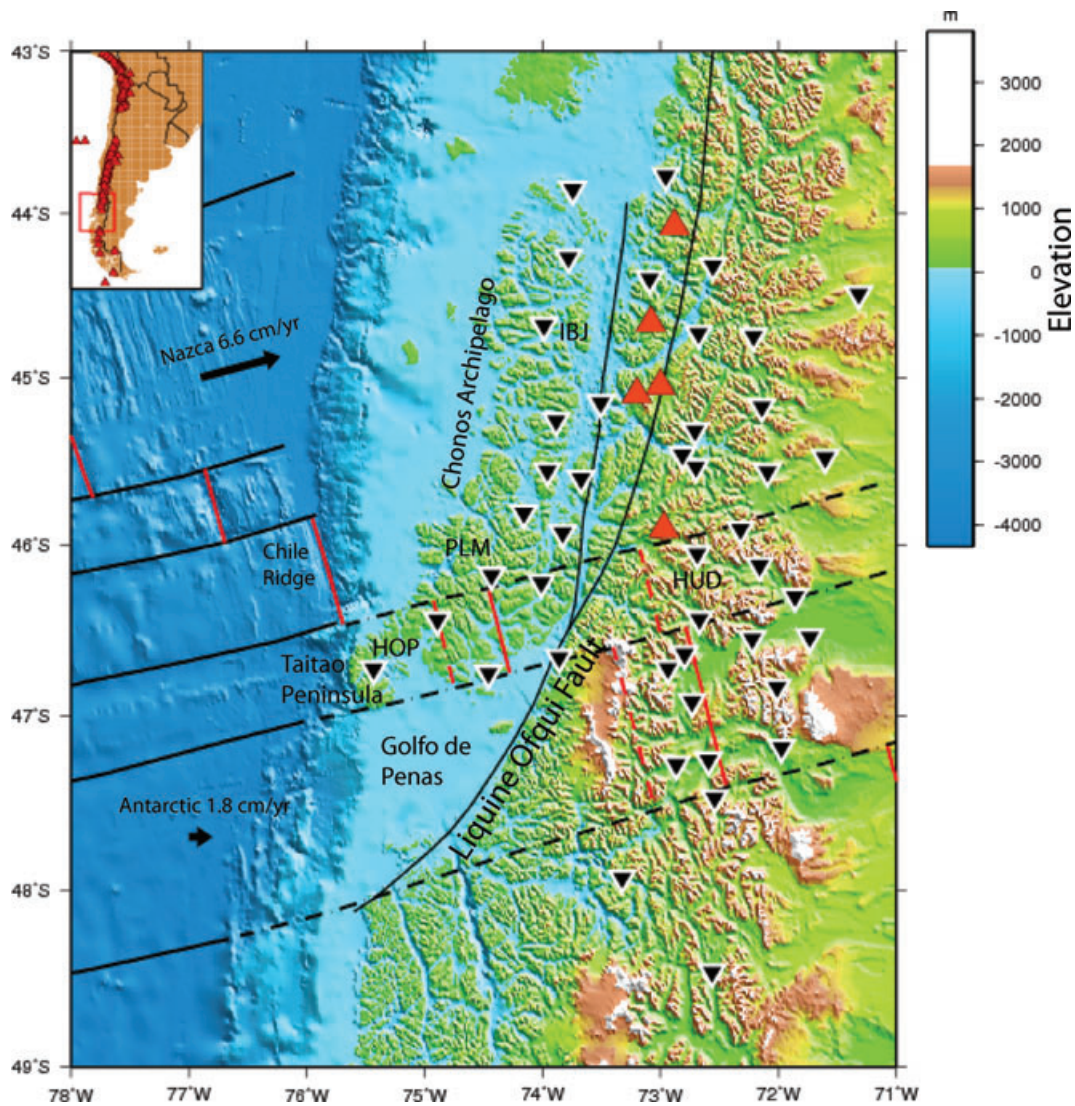
Figure 1. Tectonics and topography of Chile Triple Junction (CTJ) area: black inverted triangles, seismic stations; red triangles, volcanoes. Black and red lines: transform faults, fracture zones, and active ridge segments, dashed where subducted (surface projections). Arrows are relative convergence directions of Nazca (6.6 cm yr^{-1}) and Antarctic (1.8 cm yr^{-1}) plates (Wang *et al.* 2007). Double stranded fault cutting the region is the Liquiñe-Ofqui fault zone.

tectonics of the study area are controlled by the subduction of the actively spreading Chile Ridge (Cande & Leslie 1986; Cande *et al.* 1987), the plate boundary between the Antarctic and Nazca oceanic plates, currently subducting beneath South America at convergence rates of 1.85 and 6.6 cm yr^{-1}, respectively (Wang *et al.* 2007). Subduction of active ridge segments leads to formation of slab windows—gaps between the subducted oceanic lithospheres (Russo *et al.* 2010a)—due to continued spreading and cessation of new lithosphere production (e.g. Cande & Leslie 1986; Ramos & Kay 1992; Murdie & Russo 1999; Breitsprecher & Thorkelson 2009; Eagles *et al.* 2009). Offshore seismicity (*M* > 4), occurs on the active ridge segments and transform faults of the Chile Ridge. Onshore, seismic activity is low and the only previous seismic study realized in this area revealed a sparse alignment of slab earthquakes parallel to the subducted Taitao fracture zone, indicating continued slip on this ridge transform (Fig. 1) after subduction (Murdie *et al.* 1993). South of the CTJ the seismicity is poorly recorded and apparently even less active, perhaps owing to the slow convergence of the Antarctic plate. Between the Chonos Archipelago and the con-

tinent, the Liquiñe-Ofqui fault zone (LOFZ), the main structure of the overriding continent in this region, is an active, low-seismicity, dextral strike-slip fault, with a length of ∼1000 km extending from 40 to 47°S, running parallel to the volcanic arc (Fig. 1; Cembrano & Herve 1993; Cembrano *et al.* 1996; Rosenau *et al.* 2006; Russo *et al.* 2010b). The fault is an intra-arc shear zone related to the oblique convergence of the Nazca Plate, partitioning deformation and allowing NNE translation of a forearc sliver (Wang *et al.* 2007).

The geology of the South American plate in the CTJ area (Figs 2a and b) is divisible into four principal geological units that lie in approximately north–south belts along the subduction zone. The Western Metamorphic Complex (WMC), constitutes the primary basement outcrops in the forearc domain of the Chonos archipelago and Taitao Peninsula. In the Chonos islands, the WMC consists predominantly of metaturbidites, with some occurrences of mafic schists and metacherts (Herve *et al.* 2008). Rare preserved fossil faunas date this formation to the Late Triassic (Fang *et al.* 1998). Intercalated mica schists, phyllites and other metasediments make
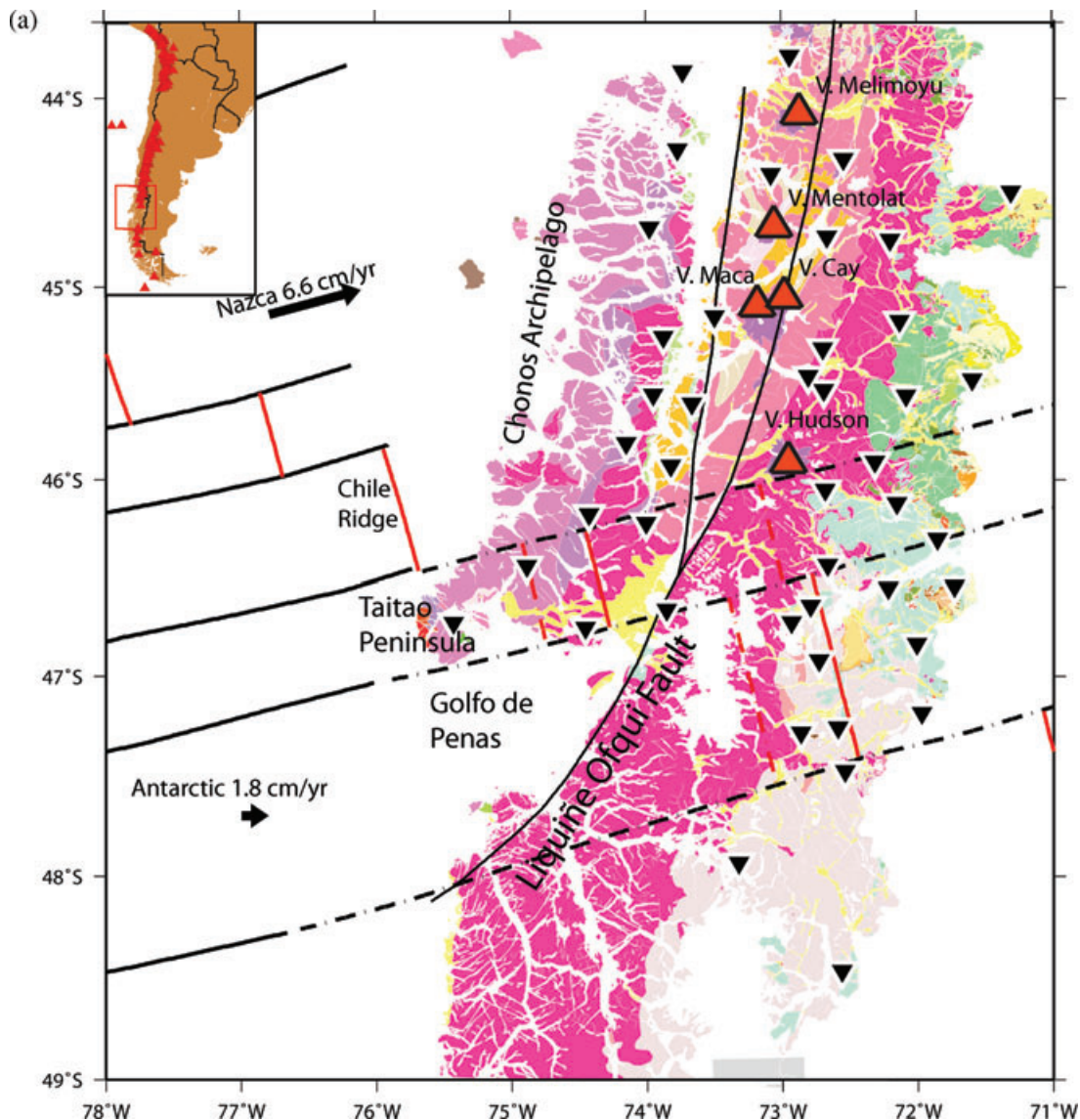
Figure 2. (a) Geological map of CTJ region, modified from Escobar (1980). Black inverted triangles are seismic stations; red triangles, volcanoes. Chile Ridge structures, Liquiñe-Ofqui fault zone, as in Fig. 1. (b) Geological units shown in (a), modified from Escobar (1980).

up the remaining WMC units (Escobar 1980). The Taitao ophiolite complex, outcropping on the westernmost tip of the Taitao Peninsula, is evidence of obduction of young Nazca Plate crust, a product of the collision between the Tres Montes segment of the Chile ridge and the overriding continent (Forsythe & Nelson 1985; Forsythe *et al.* 1986; Nelson *et al.* 1993; Lagabrielle *et al.* 1994; Shibuya *et al.* 2007).

The North Patagonian Batholith (NPB) is one of the world's largest intrusive bodies, extending quasi-continuously from 41 to 52°S, with a width of nearly 200 km. The granodiorites, granites and tonalites of the NPB are separated in two north–south bands that differ mainly in age (Pankhurst *et al.* 1999). The Miocene central band of the Northern Patagonian Batholith (MPB) outcrops continuously along the active volcanic arc north of the CTJ (i.e. ∼46° S), but does not extend south of the bifurcation of the Liquiñe-Ofqui fault. In contrast, the Lower Cretaceous North Patagonian Batholith (LCPB) outcrops throughout the study region, primarily to the east of the LOFZ, but some satellite bodies outcrop in a N–S trending belt along the easternmost Chonos islands and the Taitao

Peninsula. The LCPB extends continuously across the pronounced gap in modern arc volcanic activity (e.g. Ramos & Kay 1992), but trends NNE, and thus occupies a forearc position south of the Golfo de Penas (Figs 2a and b).

The Paleozoic Eastern Metamorphic Complex (EMC) outcrops in the SE of the study region (Fig. 2), includes the oldest rocks in the study region, and consists mainly of multiply deformed and highly compacted metamorphic rocks (quartzites, marbles, metaconglomerates and metabasalts) (Parada *et al.* 2001).

North of the EMC (∼47° S) outcrops between the LCPB and the Chile–Argentina border, faulted and folded Jurassic and Tertiary felsic and intermediate volcanics and sedimentary rocks of the Patagonian Ranges outcrop both north and south of the current CTJ (Escobar 1980; Lagabrielle *et al.* 2004, 2007). A suite of Tertiary basalts erupted above the Patagonian Range units in Chile, but much more extensively in Argentina, are thought to represent a shift of magmatic activity—normally expressed at the arc—to the backarc region, where extensive Neogene plateau lavas have erupted synchronously with ridge segment subduction (Ramos & Kay 1992;

(b) Sedimentary Sequences

Pleistocene-Holocene
Aluvial, glacial, deltaic, coastal deposits.

Volcano-Sedimentary Sequences

Lower Cretaceous
Volcanic sequences. Basaltic to andesitic lavas and breccias, andesitic
to rhyolitic pyroclastic rocks and sedimentary intercalations. Patagonian Range.

Jurasic
Volcanic sequences and centers : dacitic to rhyolitic pyroclastic rocks,
andesitic lavas and sedimentary intercalations. Patagonian Range.

Volcanic Rocks

Quaternary
Stratavolcanoes and volcanic complexes: basaltic to rhyolitic lava,
domes and andesitic to basaltic pyroclastic deposits. Patagonian Range.

Miocene
Serpentinite, gabbro, dikes and pillow lava with limonite intercalations.
Taitao ophiolite.

Intrusive Rocks

Miocene (MPB)
Granodiorite, diorite, tonalite. Central part of North Patagonian Batholith.

Lower Cretaceous (LCPB)
Granite, granodiorite, tonalite. North Patagonian Batholith.

Metamorphic rocks

Triasic (WMC)
Mica schist, phyllites, metasedeminataries. Western Metamorphic
Complex.

Triasic (WMC)
Metaturbiditic sequence. Western Metamorphic Complex.

Devonic-Carboniferous (EMC)
Metasandstone, phyllites, marble, chert, metabasalt, metaconglomerate.
Eastern Metamorphic Complex.

Figure 2. (*Continued.*)

Gorring *et al.* 1997; Espinoza *et al.* 2005, 2008; Guivel *et al.* 2006).

Pleistocene–Holocene strato volcanoes built atop the MPB/LCPB, forming the southern part of the Southern Volcanic Zone (SVZ; Ramos & Kay 1992; Gorring *et al.* 1997), are closely aligned with the trend of the LOFZ (Cembrano *et al.* 1996). Within the study region, five major strato volcanic centres have been active during Holocene-Recent: Melimoyu (200 ± 75 AD), Mentolat (1710 ± 5 AD), Maca (410 ± 10 AD), Cay (Holocene) and Hudson (1991). Hudson is the southernmost volcano of the SVZ, coincident with the CTJ. Between the SVZ and the Austral Volcanic zone (AVZ) south of the study area, a gap of about 500 km is thought to be a result of perturbations in the upper mantle wedge beneath South America caused by subduction of the Chile Ridge and slab window formation (Cande & Leslie 1986; Ramos & Kay 1992; Russo *et al.* 2010b). Gravimetric studies show a low gravity anomaly in this area, bounded on the west by the LOFZ (Murdie *et al.* 2000). Structural analyses of these units show a marked change in late Cenozoic deformation patterns, and uplift, possibly ongoing, related to subduction of the Chile Ridge (Lagabrielle *et al.* 2004, 2007).

2 DATA

We used ambient seismic noise data obtained from 44 broadband sensors (Fig. 1) deployed between 2004 December and 2007 February in the CTJ region, as part of the joint Universidad de Chile–University of Florida Chile Ridge Subduction Project. Unlike other parts of the Andes, seismic activity near the CTJ is rare, with an almost complete absence of events larger than magnitude 4 between the network installation and January 2007 (Russo *et al.* 2010a,b). Thus, the study area is a nearly ideal place for

tomography derived from ambient seismic noise. The area is very remote and sparsely inhabited, so cultural noise is also virtually non-existent. We analysed continuous broad-band vertical component seismic data recorded at 50 samples per second at the CRSP stations during the period from 2004 December to 2007 January. For each station pair, we used a minimum of 30 d and a maximum of 1 yr (2006) of continuous data. Because some of the CRSP stations did not operate during the entire deployment, only 38 station pairs met the requirement of more than 30 d of simultaneous recording. This limitation yielded 703 ($38 \times 37/2 = 703$) interstation paths traversing an area approximately of 400×700 km, including the CTJ forearc, arc and backarc regions.

3 METHODOLOGY

3.1 Cross-correlation of noise

All signals were bandpass filtered at periods of 2.5–100 s, downsampled to 0.5 s, detrended, and demeaned. We then performed a single-bit binarization of the signals, retaining just the sign of the signal amplitude (+1 for positive, −1 for negative). This truncation is effective in reducing the influence of any local earthquakes or noncoherent noise included in the time window that could potentially modulate the interstation cross-correlation (Campillo & Paul, 2003; Bensen *et al.* 2007). The spectra (Fig. 3) of the cross-correlated signals show peaks between 7 and 10 s, due to the influence of ocean noise on the resulting Green's function, and we added white noise to the data to flatten the spectra.

24 hr of data for each station pair were cross-correlated independently and then stacked day by day into one time-series that represents the Green's function dominated by Rayleigh wave energy for the given station pair. The time-series were bandpass filtered at 5–10, 10–20 and 20–30 s and normalized by the maximum amplitude, and the maximum amplitude of the envelope calculated, yielding the group velocity waveform of the scattered Rayleigh wave travelling from one station to the other. The cross correlation thus also yields the interstation traveltime of forward and (in some cases) reverse propagating surface waves, as discussed above.

We used two time-series for stations HOP and HUD, located to the west and in the centre, respectively, of the CRSP network to illustrate the cross-correlation technique. Station HOP (Fig. 4a) was located at the western extreme of the network on the Taitao Peninsula. Its cross-correlated signals with all other stations each show a strong causal, forward-propagating wave, indicating ocean waves were the principal source of the long period noise generating the interstation Rayleigh waves. For each of these interstation cross-correlograms, the amplitude of the anticausal back-propagating wave is very small and difficult to observe, but when visible, symmetric in time with the forward propagating scattered wave. We observe that lag time increases as a function of the station pair distance. Cross-correlograms for station HUD (Fig. 4b), located at the centre of the network, show causal correlations along paths to stations located to its east, and also to those lying to its west, and the anticausal, backpropagating scattered waves are small but symmetric.

To quantify the effect of our sensor distribution in our results (Fig. 5), we plotted the number of station-pairs as a function of azimuth for distances between 0–100, 100–200, 200–300 and 400–500 km. Most of the paths trend north–south, but this trend is more prevalent for short paths (<300 km). Longer paths tend to yield a wave velocity that is an average of the crustal heterogeneity, whereas short paths yield in more variable velocities because averaging of structures is less along shorter paths.

The interstation velocities, determined from the interstation distances and traveltimes, (Figs 6a and b) converge to the average crustal velocity as distance increases, as expected, but are more scattered for short distances. We also observe a bias toward high velocities for short paths, relative to velocities less than the average that cannot be explained by the station distribution. In part, these highly dispersed values result from low signal-to-noise ratio (SNR; Figs 6e and f) for long-wave periods (20–30 s) which are not well developed in short station path and short-wave periods (5–10 s) attenuated at long distances.

The interstation velocities (Figs 6c and d), vary more for paths trending north–south than for other azimuths. The main source of seismic noise in this region is ocean waves along the N–S trending coast, which produces larger amplitude scattered waves along paths trending E–W than N–S. Correlations are thus stronger for E–W trending interstation paths. As shown below, once SNR is taken into account, this velocity variability with path azimuth is minimized.

3.2 Signal-to-noise ratio

Following Gerstoft *et al.* (2006), we estimated the quality of the signal for the three period bands via a SNR, defined as the ratio between the maximum amplitude of a 50 s window centred at the time of the main scattered arrival, and the standard deviation of a 50 s window centred 475 s before the arrival time (i.e. true noise only). The SNR was calculated for both the causal and acausal sides of the time-series. Plots of SNR versus velocity (Figs 6e and f) show that calculated interstation velocities are more variable for low SNR ratio (<6) signals, which result predominantly for long period (20–30 s) correlations. Signal quality is highest for shorter periods (5–10 s). With respect to interstation path azimuth, SNR (Figs 6g and h) is high for stations pairs trending east–west. SNR is high for paths trending W (270° in Fig. 6g) and E (90° in Fig. 6h), depending on which station of the cross-correlation pair is nearer the coast.

In order to minimize the effects of low SNR cross correlations in the traveltime inversion, we selected station pairs with SNR values larger than 6. From the waveforms we selected the positive or negative lag (causal or acausal) with maximum SNR. We require the interstation distance to be greater than 1.5 times the wavelength (λ) of the highest cut-off period ($\tau = 10$, 20 and 30 s), and assuming a phase velocity, c, of 4 km s^{-1} (Bensen *et al.* 2007), the minimum path lengths are 60 km for the 5–10 s band, 120 km for 10–20 s waves and 180 km for 20–30 s waves. The velocities of the interstation pairs retained after discarding the low SNR correlations (Fig. 7) are considerably smoother with respect to path azimuth. However, a systematic variation of crustal velocity with path azimuth is visible in Fig. 7: the highest velocity paths trend N–S (around 0° and 180° azimuth) for the longest period waves (blue). This variation is a consequence of the sensor distribution (Fig. 5) and possibly also azimuthal anisotropy in the crust (Murdie & Russo 1999; Gallego *et al.* in preparation). Of the 703 potential interstation paths, we retained 640 5–10 s wave paths with an average velocity of 3.0 km s^{-1} and a variance of 0.02, 454 10–20 s wave paths with mean velocity of 3.1 km s^{-1} and a variance of 0.01, and 200 20–30 s wave paths with mean velocity and variance of 3.2 km s^{-1} and 0.05. Note that the longer period waves are more sensitive to higher seismic velocities of the deeper crust.
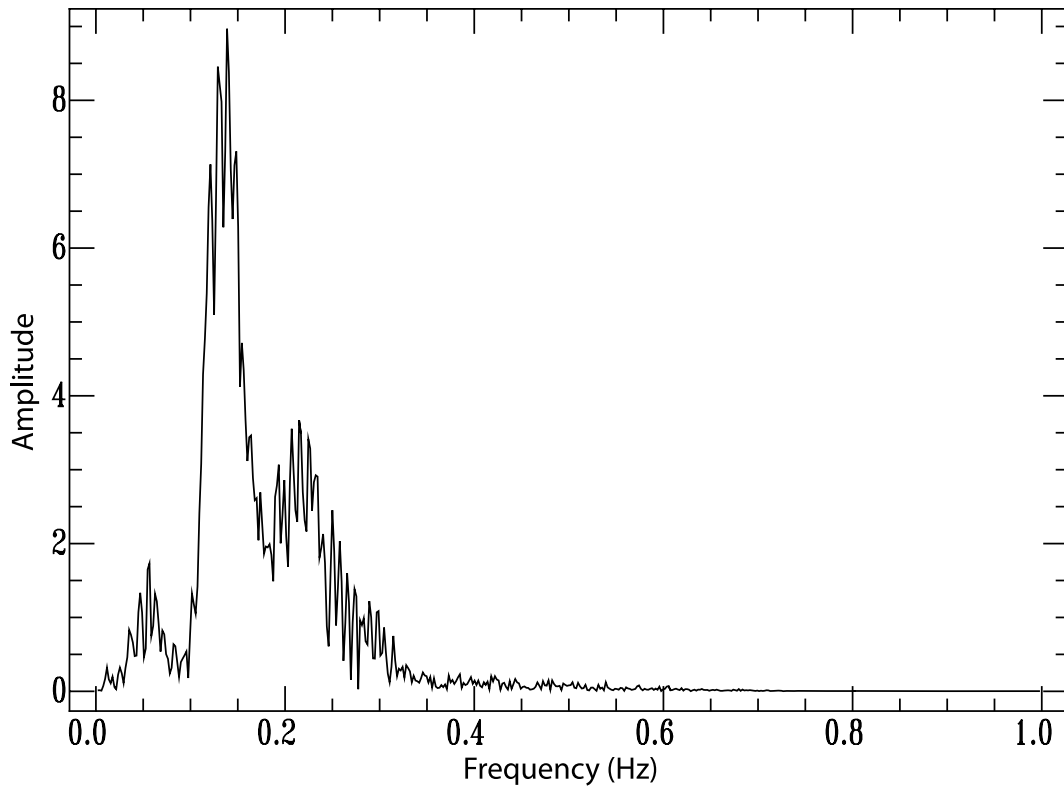
Figure 3. Frequency analysis of cross-correlated waveform between station PLM and IBJ.

3.3 Dispersion and Rayleigh wave group velocities

Next, we performed a frequency–time dispersion analysis (FTAN) to estimate group velocity as a function of period and the sensitivity of the period wave to the depth (Fig. 8). We implemented the method of Levshin *et al.* (1992). First, the cross-correlated signal was transformed to the frequency domain, and the spectrum was flattened and normalized by weighting the complex signal by the smooth amplitude spectrum. Then, we calculated the analytical signal that discard the negative frequencies with no loss of information (Bensen *et al.* 2007):

$$S_a = s(\omega)[1 + \text{sgn}(\omega)] \qquad \text{sgn} = \begin{cases} j & \omega > 0 \\ -j & \omega < 0 \end{cases}. \qquad (1)$$

For each station-pair waveform, we filter the signal in a narrow band using a Gaussian filter.

$$F(\omega - \omega i) = \exp\left[-\alpha_i \left(\frac{\omega - \omega\iota}{\omega_i}\right)^2\right] \qquad i = 1, \ldots, N, \qquad (2)$$

where ω_i is the central frequency for periods between 5 and 30 s with intervals of 1 s, and α is the relative width of the filter, which is distance dependent. The dispersed signal is constructed by weighting the analytical signal with the Gaussian filter

$$S_a = s(\omega)[1 + \text{sgn}(\omega)]F(\omega - \omega_i). \qquad (3)$$

The resulting waveform was transformed to the time domain and the logarithm of the symmetric signal calculated, averaging the positive and negative lagged signals, thereby yielding a matrix with period and group velocity arrival time. To find values between grid points we apply a spline interpolation.

The dispersion curve is obtained from the local maxima for each period. To eliminate spectral holes in the dispersion curves, we used the local maximum in a time window of 30 s centred around the maximum of the previous period. We disregarded curves with large velocity jumps and gaps, finally obtaining a total of 407 dispersion curves (Fig. 9). The averaged group velocity of the dispersion curve for each period was used to estimate a 1-D velocity model (Fig. 10). We used an iterative weighted inversion method (Herrmann & Ammon 2002). The initial model was constructed with 11 5 km thick layers, each with constant $Vs = 3.5$ km s^{-1}, $Vp = 6$ km s^{-1} and density $= 2.5$ kg m^{-3}. The sensitivity of the wave period with respect to the crustal depth (Fig. 11) was estimated using the derivative of the calculated model with respect to the initial model.

3.4 2- D traveltime inversion

We used the method of Tarantola (2005) to perform a 2-D traveltime inversion. The area was parametrized as cells of 30×30 km. Wave propagation paths were assumed to be straight lines, given the small effect of earth curvature at these propagation distances. We estimated the forward velocity model by inverting the linear model, $\mathbf{d} = \mathbf{Gm}$, where $\mathbf{G}$ contains the lengths of segments formed by the intersections of ray paths and the cell boundaries, $\mathbf{m}$ is the matrix of slownesses of each cell block and $\mathbf{d}$ is the interstation traveltime, obtained from the cross-correlation of stations pairs. The new model is obtained by solving the inverse problem

$$\mathbf{m} = \mathbf{m}_{\text{prior}} + C_M G^t (G C_M G^t + C_D)^{-1}(\mathbf{d} - \mathbf{Gm}_{\text{prior}}), \qquad (4)$$

where $\mathbf{G}^t$ is the transpose of $\mathbf{G}$, $\mathbf{m}_{\text{prior}}$ is the *a priori* velocity model, assumed constant with values of 3.0 km s^{-1} for the 5–10 s period
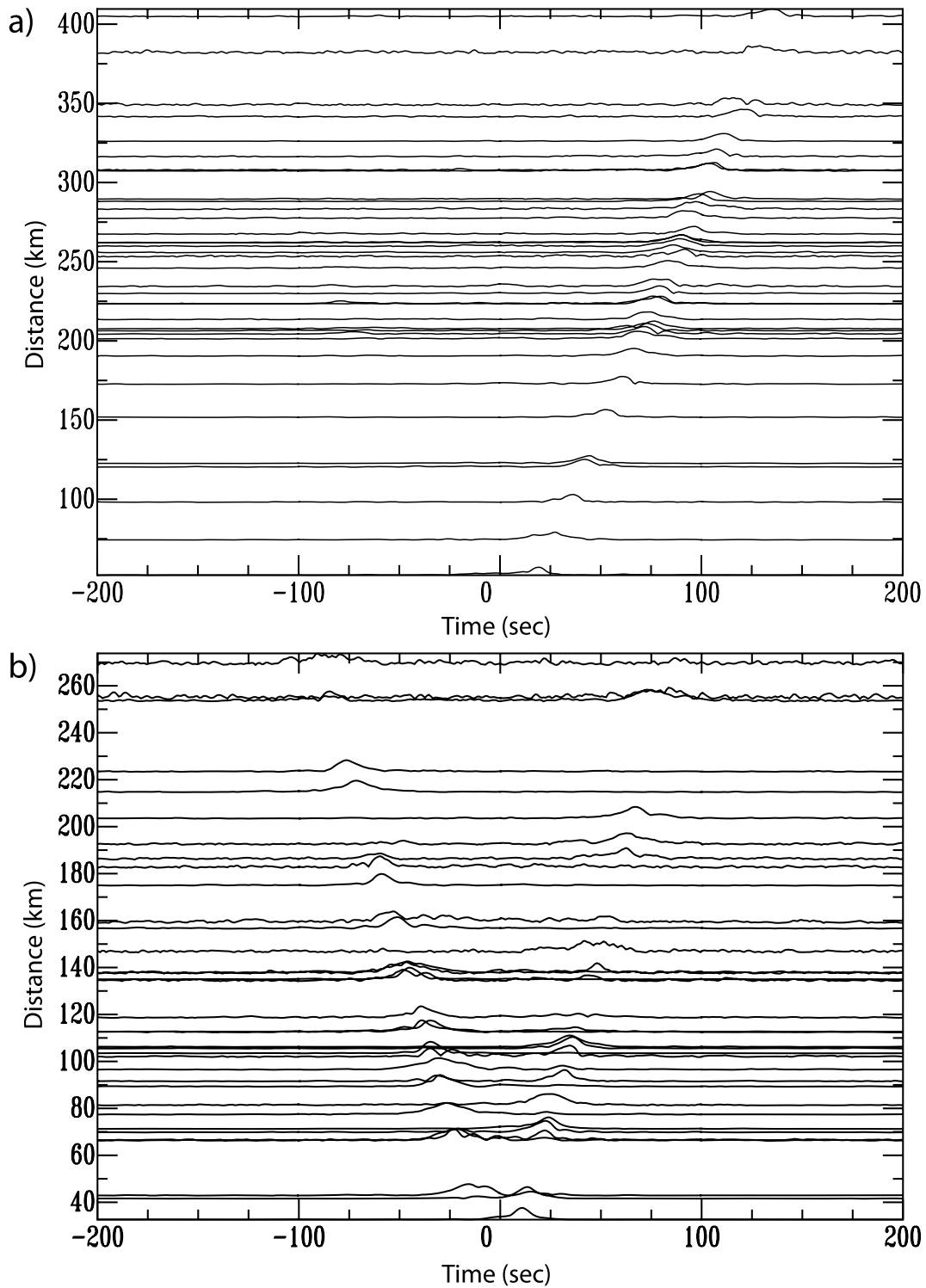
Figure 4. (a) Time-series of cross-correlation for station HOP01, located at the extreme west of the study area, near the coast, and other CRSP stations. Signal was bandpass filtered at 2.5–10 s. (b) Time-series of cross-correlation for station HUD01, located approximately at the centre of the CRSP network. Signal was bandpass filtered at 2.5–10 s.

correlograms, and 3.1 km s^{-1} for those of the 10–20 s period signals. $\mathbf{C_D}$ is a diagonal matrix of traveltime errors (assumed to be 2 s), and $\mathbf{C_M}$ is the covariance matrix, derived from the exponential covariance function

$$C(x, x') = \sigma^2 \exp\left(\frac{-\|x - x'\|^2}{L}\right),$$ (5)

where σ is the variance of the velocity, $(x-x')$ is the distance between cells and L is the smoothness, assumed to be 20 km, of the variation between contiguous cells. For large distances, the covariance tends to zero. The resolution matrix is

$$R = (G^t C_D^{-1} G + C_M^{-1}).$$ (6)
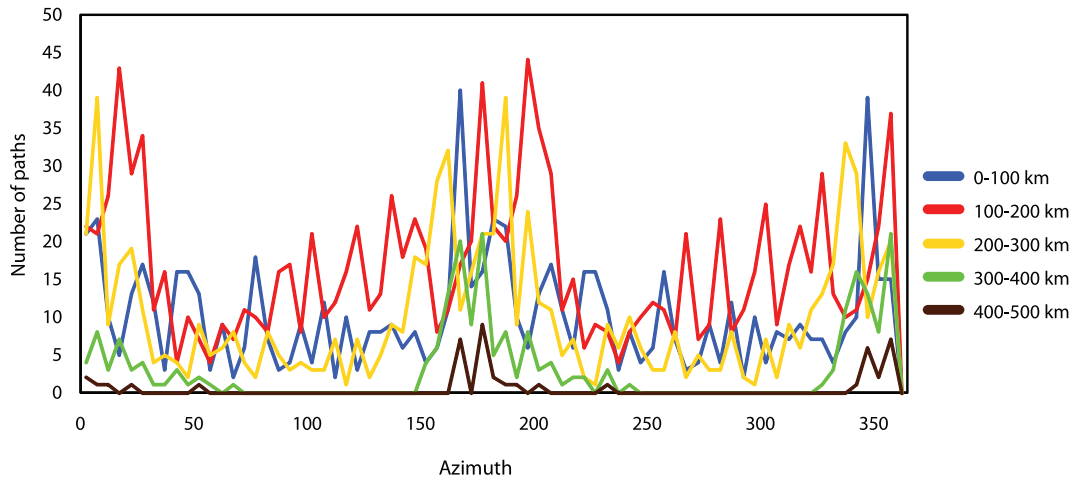
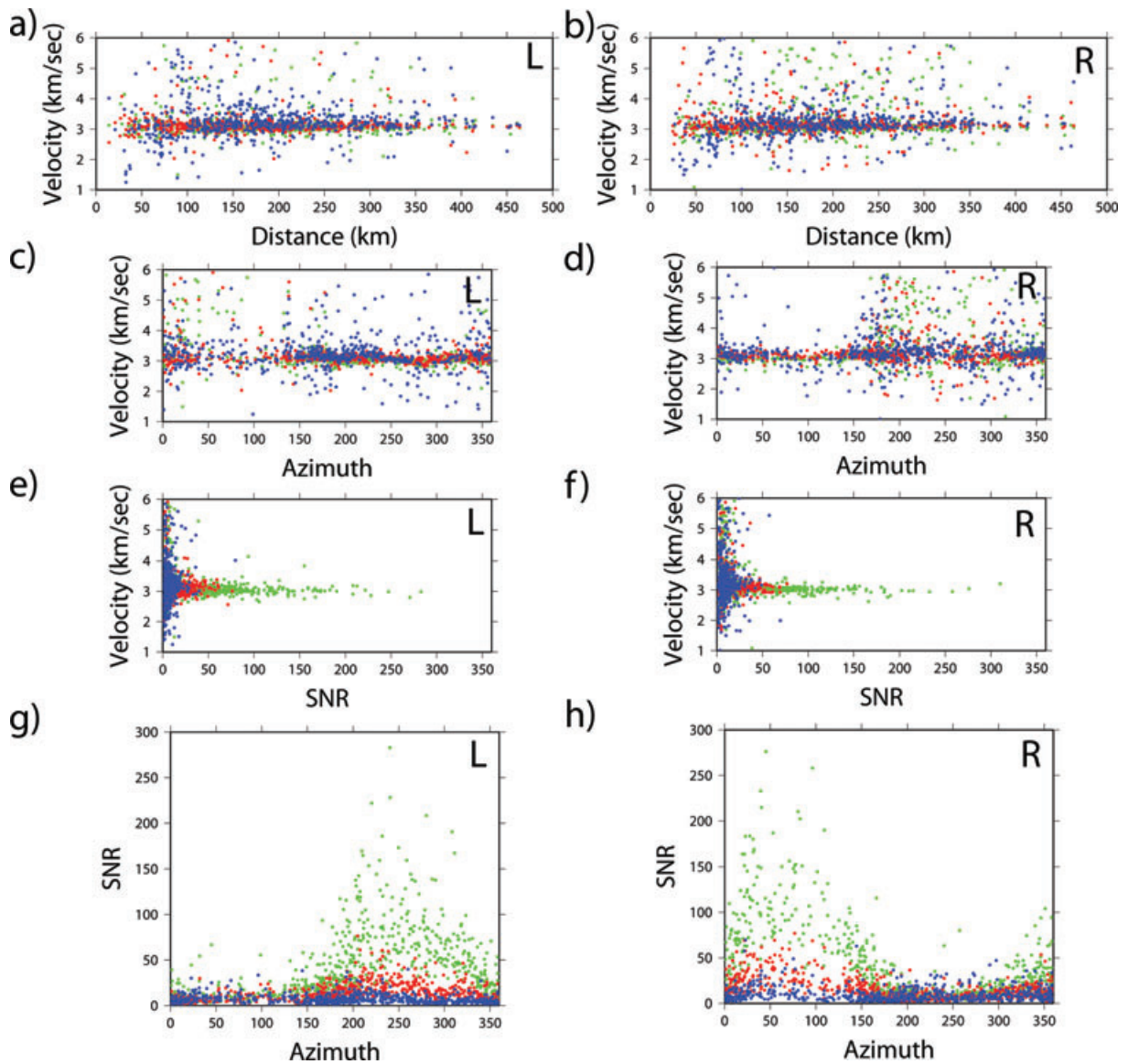**Figure 5.** Azimuthal distribution of station paths for distances between 0 and 500 km.

Figure 6. Data analysis for positive and negative lags of the cross-correlation for three period bands: 5–10 s (green dots), 10–20 s (red dots) and 20–30 s (blue dots). (a–b) Average group velocity for station pairs as a function of distance. (c–d) Average group velocity for station pairs as a function of azimuth. (e–f) Average group velocity as a function of SNR. (g–h) SNR as a function of azimuth.
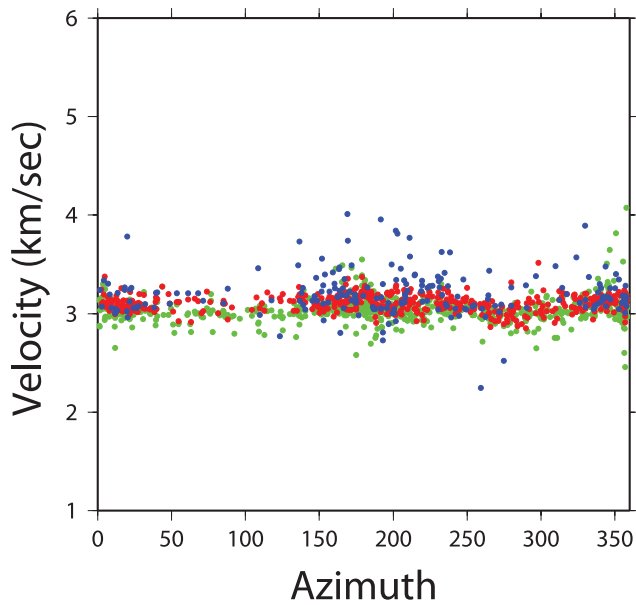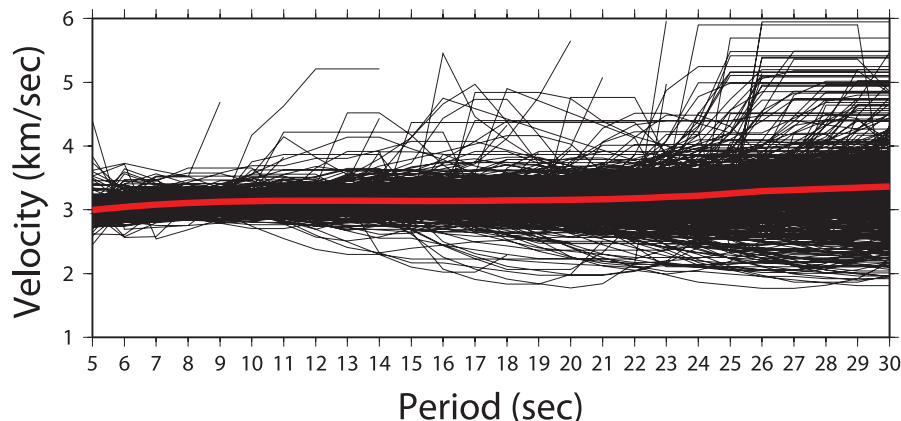
Figure 7. Selected group velocities for station pairs with SNR > 6 and distance >1.5 times the wavelength of the filter.
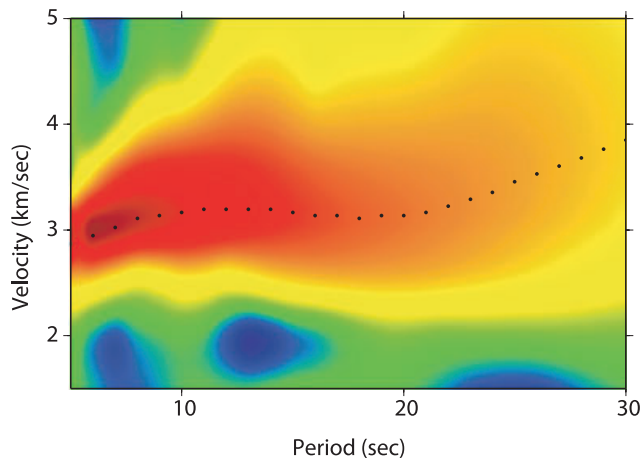
Figure 8. FTAN analysis for IBJ-PLM station pair; red colours indicate high amplitude of the cross-correlation after the Gaussian filter. Black dots indicate the highest amplitude for each period band.

We thus produced two 2-D models for the selected cross-correlated waveforms at 5–10 and 10–20 s period. 640 ray paths were used for the 5–10 s inversion (Fig. 12a) and 454 paths for 10–20 s model (Fig. 12b). Ray density is higher at the centre of the network, which is evident in the maps of inversion resolution (Figs 13a and b). Resolution falls below the acceptable threshold only near the edges of the CRSP network. The velocity model for 5–10 s band (Figs 11 and 14a) corresponds to the shallow crust above 10 km, and that derived from the 10–20 s band is representative of crustal structure between 10 and 20 km depth (Figs 11 and 14b).

### 3.5 3-D traveltime inversion

We also calculated a 3-D velocity (Fig. 15) model using the 407 dispersion curves derived from the group velocity analysis (Fig. 9). For each period band between 5 and 20 s, we inverted the traveltimes (Tarantola 2005), obtaining 25 velocity models. For each cell we inverted the 25 group velocities (Hermann *et al.* 2002) using the initial 1-D model (Fig. 10) calculated from the averaged group velocity of the dispersion curve, obtaining a 3-D model of the velocity perturbation respect to the initial model.

4 RESULTS

Rayleigh wave group velocities for 5–10 and 10–20 s period bands are shown in Figs 14(a) and (b), respectively. *S*-wave velocities from the surface wave dispersion analysis are shown in Fig. 15, and the 1-D *S*-wave crustal model for the study area is shown in Fig. 10. The 1-D crustal model (Fig. 10) shows a velocity increase from 3.2 to 3.6 km s^{-1} between 0 and 20 km depth, and a deeper increment of velocity from 3.6 to 3.9 km s^{-1} could indicate a Moho depth of 30–40 km, but resolution deeper than 30 km is poor (Fig. 11).

4.1 5–10 s period inversion

The principal features visible in the map of group velocities derived from the 5–10 s period (Fig 14a) signals are an elongated low velocity (2.8–3.0 km/s) anomaly approximately between the two branches of the LOFZ between 44.5 and 45.5°S; and patches of low (2.6–2.8 km s^{-1}) velocity at the NE edge of the Golfo de Penas and extending to the east; and along the Chile–Argentina border between 45 and 47°S, along the eastern edge of the study region. Shallow crustal velocities in the western Chonos Islands and Taitao Peninsula are generally low, but the eastern part of this

Figure 9. 407 dispersion curves (black) and the averaged group velocity at each period (red).
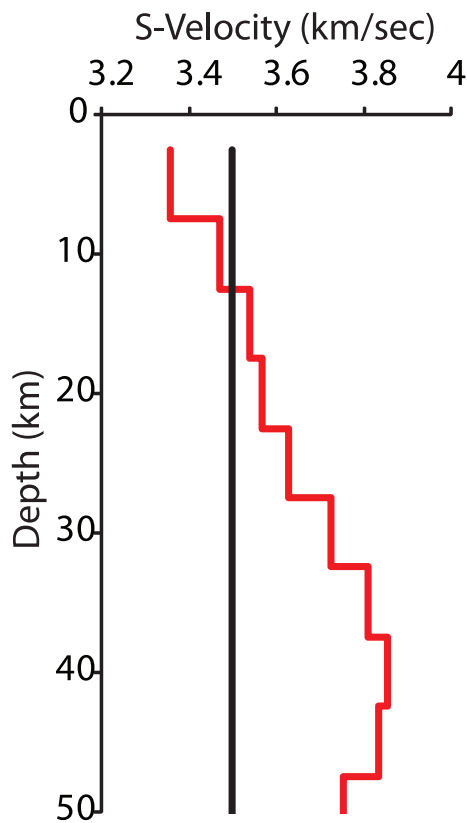
Figure 10. 1-D inversion model (red line) for the averaged dispersion curves; the initial model (black line) is a constant $Vs = 3.5$ km s^{-1}.

area is marked by higher velocity anomalies (3.0–3.2 km s^{-1}). More restricted regions of relatively high velocity (3.2–3.6 km s^{-1}) occur in three small areas near the centre-north of the map, and near the southeastern boundary of the region of resolved velocities. In general, the region lying 100–150 km to the east of the LOFZ is characterized by relatively high velocities of 3.1–3.3 km s^{-1}.

4.2 10–20 s period inversion

Fig. 14(b) shows the results for group velocities determined from the 10–20 s period signals. The overall pattern of velocity anomalies is similar to those visible in Fig. 14(a), although the range of velocities is more restricted (2.8–3.3 km s^{-1}), and the scale of the anomalies appears to be smaller. Two high velocity anomalies (3.1–3.3 km s^{-1}) lie parallel to the Lower Cretaceous North Patagonian Batholith, and a low velocity (3.0 km s^{-1}) anomaly occurs where the volcanic arc is present. The Taitao Peninsula is also marked by low velocity (<2.9 km s^{-1}). Note the persistence of a high velocity (3.1–3.2 km s^{-1}) anomaly at the southeastern edge of the study area, and a low velocities (2.9–3.1 km s^{-1}) along the Chile–Argentina border between 45 and 47°S.

4.3 3-D Group velocity inversion

The 3-D model (Fig. 15) obtained from the dispersion analysis is in a good agreement with the two 2-D models. A high velocity anomaly is present between 2.5 and 20 km depth along the LPBC, and patches of lower velocity anomalies follow the volcanic arc and the LOFZ. The low velocities along the eastern edge of the study area fade with
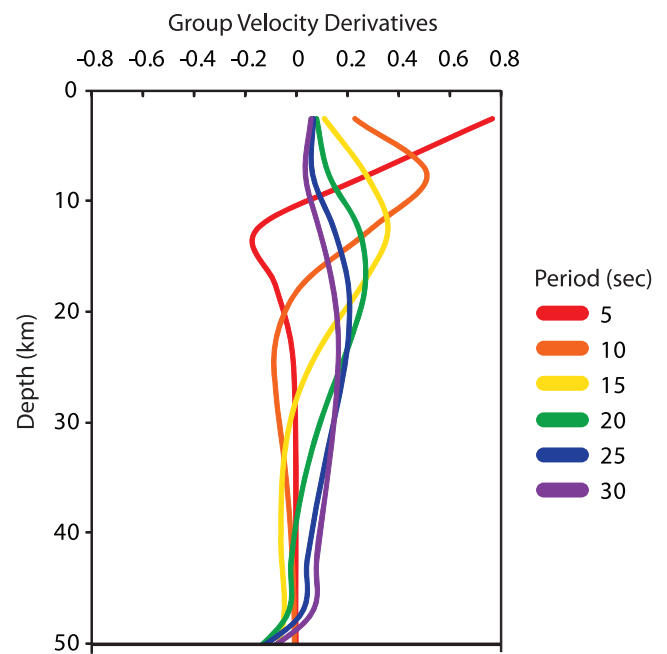
Figure 11. Group velocity derivatives of the calculated model with respect to the initial model.

depth. The extended low velocity at the Taitao Peninsula is present between 2.5 and 7.5 km, and low velocities anomalies beneath the Golfo the Penas also fade out at deeper levels.

5 DISCUSSION

Relative to other studies using the ambient seismic noise tomography technique, we find Rayleigh wave group velocity anomalies that are somewhat high. For example, Shapiro *et al.* (2005) show velocities for 7.5 s period Rayleigh waves in southern California that range from 1.4 to 4.0 km s^{-1}, with a definite preponderance of regional velocity anomalies at the low end of their scale (see their fig. 2). Similarly, Lin *et al.* (2007; see their fig. 11) show Rayleigh wave group velocities ranging from 1.8 to 3.2 km s^{-1} for 8 and 13 s period waves recorded in New Zealand. In part, such differences may be due to differences in the analysis and inversion methods. However, we note that the geology of our study area—dominated by the glacially stripped basement of Patagonian Batholiths at the surface—is distinctive and clearly lacks the extensive, deep sedimentary basins found in southern California and New Zealand. Also, Shapiro *et al.* (2005) find group velocities in the Sierra Nevada Batholith that are as high or higher than the values we find for the LCPB (3.1–3.3 km s^{-1}).

The Rayleigh wave velocities we obtained from traveltime inversions of ambient noise cross-correlations and dispersion analysis correspond closely to known geological features (Fig. 2). The inversion of the 5–10 s period Green's functions (Figs 13a and 14a) is more sensitive to shallow structure no deeper than 10 km (Fig. 11), and should therefore correlate most closely with superficial geology. We observe an elongated, north–south trending low velocity anomaly that coincides with the MPB and the Southern Volcanic Zone eruptive centres north of the CTJ. This low velocity anomaly is also bounded by the two main strands of the LOFZ (Fig. 14a). Velocities ~2.7–2.8 km s^{-1}, although not very low with respect to results from similar studies elsewhere (e.g. Lin *et al.* 2007), are noticeably low for the CRSP study region. The depth of magma
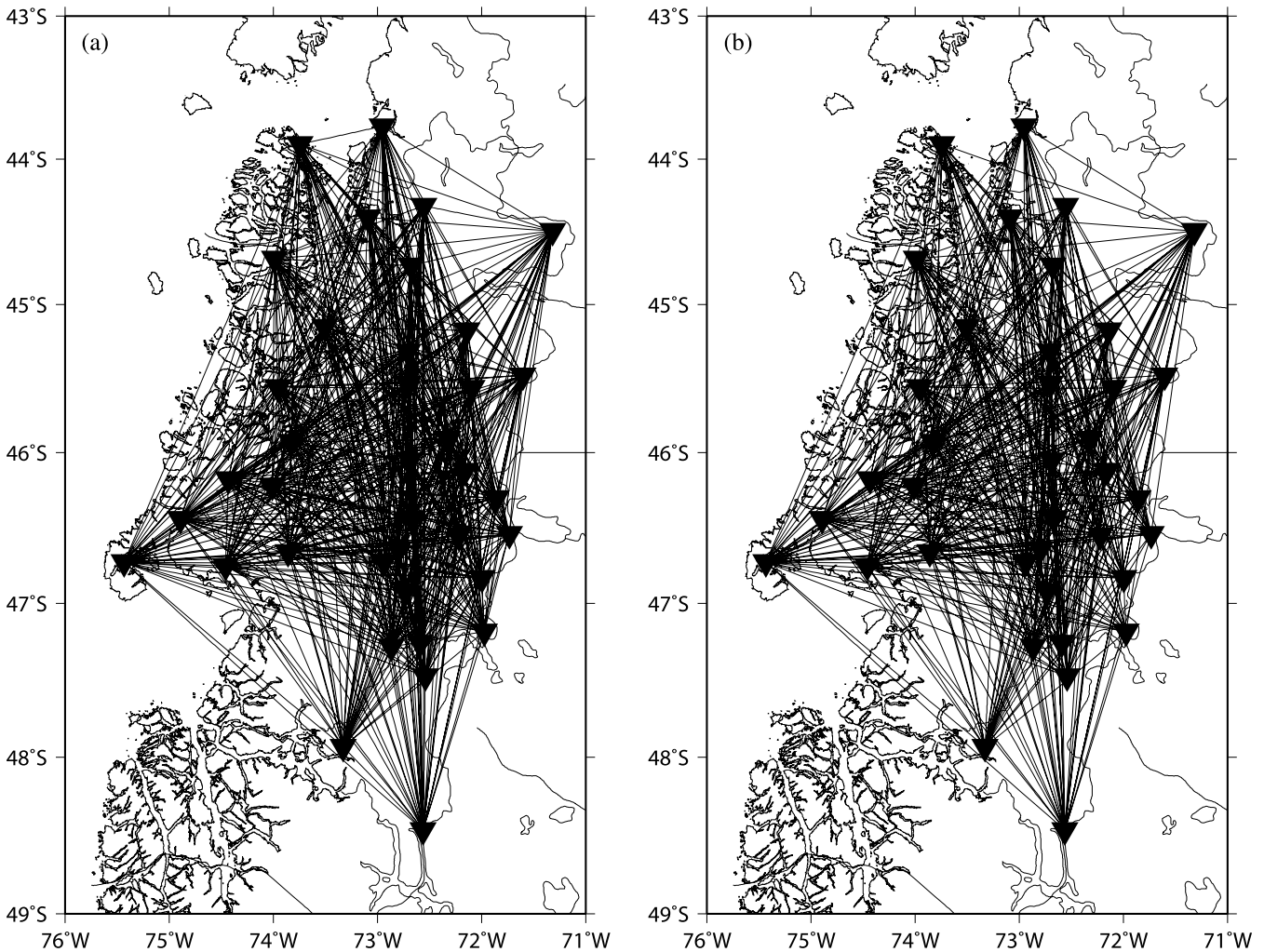
Figure 12. (a) Interstation paths for group velocities derived from Green's functions filtered at 5–10 s period. A total of 640 paths were selected. (b) Interstation paths for group velocities derived from Green's functions filtered at 10–20 s period. A total of 454 paths were selected.

chambers beneath the five arc volcanoes is uncertain, but hypocentres of earthquakes that occurred during the last eruption of Hudson volcano in 1991 were clustered between 2 and 20 km depth (Naranjo *et al.* 1993). High velocities west and east of the LOFZ correlate well with the exposures of the NPB in the eastern Chonos Islands/Taitao Peninsula and east of the LOFZ. The high velocity anomaly at the southestern corner of the study area corresponds to the metamorphic units of the Devonian-Carboniferous EMC exposed at high elevations around Monte San Lorenzo (3700 m).

The notable low velocity anomaly at the NE edge of the Golfo de Penas is probably due to the one sedimentary basin extant in the study area, as this area is clearly the site of much recent glacial sediment fill brought to the Golfo by the rivers draining Campo de Hielo Norte, the northern Patagonian ice field; the extension of this anomaly to the east correlates with the presence of the ice field. The low velocity regions near the Chile–Argentina border in the NE part of the study area (Fig. 14a) correlate with the Jurassic-Cretaceous units of the Patagonian Ranges.

The inversion of the 10–20 s period signals (Figs 13b and 14b) is sensitive to depths between 10 and 20 km (Fig. 11). We note that the observed velocity variations for this inversion are less pronounced than those of the shorter periods, perhaps indicating a more homo-

geneous crust at these depths, or, alternatively, greater smoothing of velocity heterogeneities due to longer sampling period. The high velocity anomaly in the southeastern portion of the study region, also observed in the shallower crustal velocity model, persists at these greater depths, indicating that the high velocity units of the EMC outcropping at the surface in the vicinity of Monte San Lorenzo extend throughout the upper crust (Thompson & Herve 2002).

Two high velocity anomalies (3.1–3.4 km s^{-1}) at the east and west of the volcanic arc correlate with the LCPB, indicating the presence of the batholith at depth. Lower velocity between these two features correlates with the location of the volcanic arc (Fig. 14b). The low velocity anomaly (2.7–2.9 km s^{-1}) at the Taitao Peninsula is likely a result of elevated temperatures (manifested as active hydrothermal springs and recent volcanism) due to the subduction of an actively spreading segment of the Chile Ridge (Lagabrielle *et al.* 2000).

5 CONCLUSIONS

We used cross-correlation of ambient seismic noise recorded in the CTJ region to estimate interstation time-domain Green's functions, and we inverted the resulting interstation traveltimes to obtain a crustal shear wave velocity model. Our results show that observed
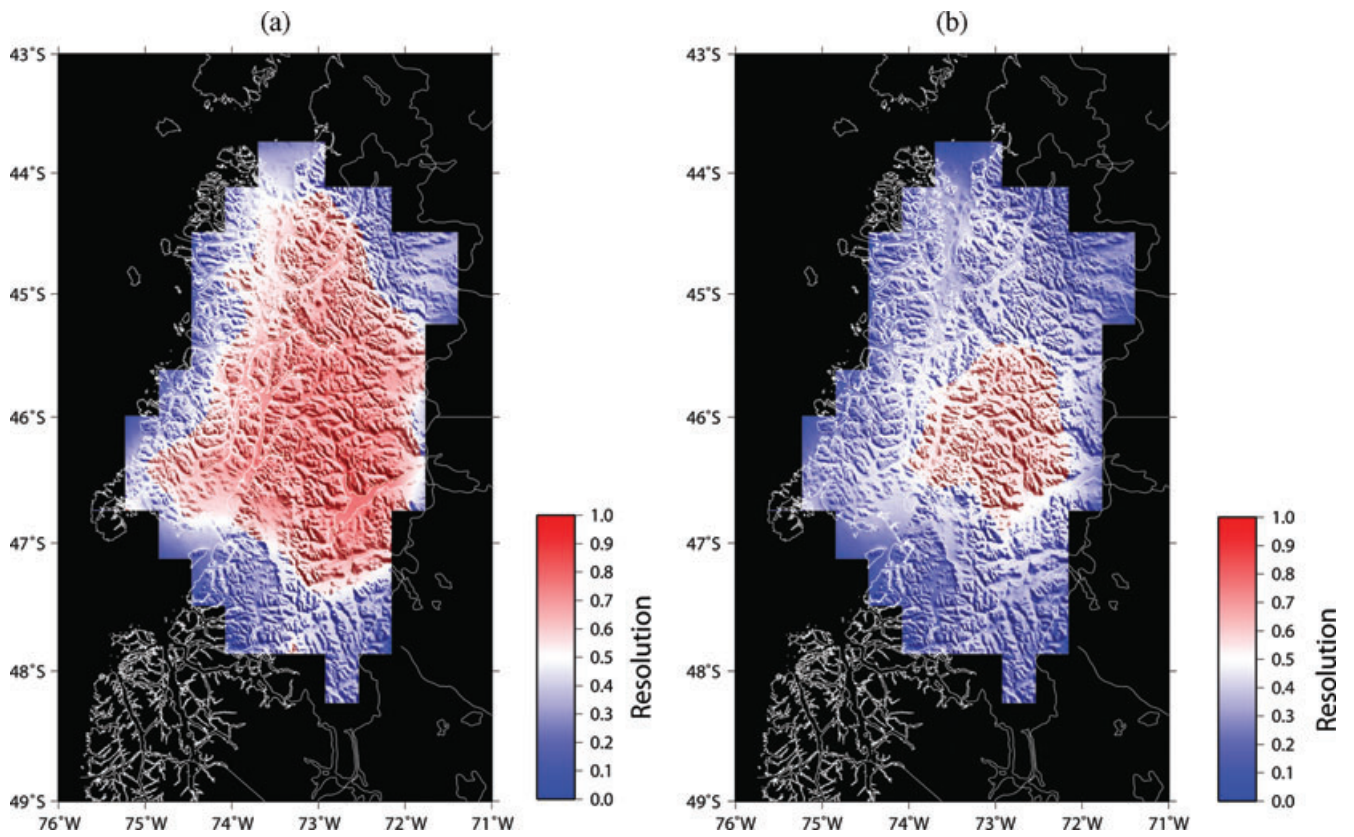
Figure 13. (a) Resolution map for 5–10 s period group velocities. (b) Resolution map for 10–20 s period group velocities.
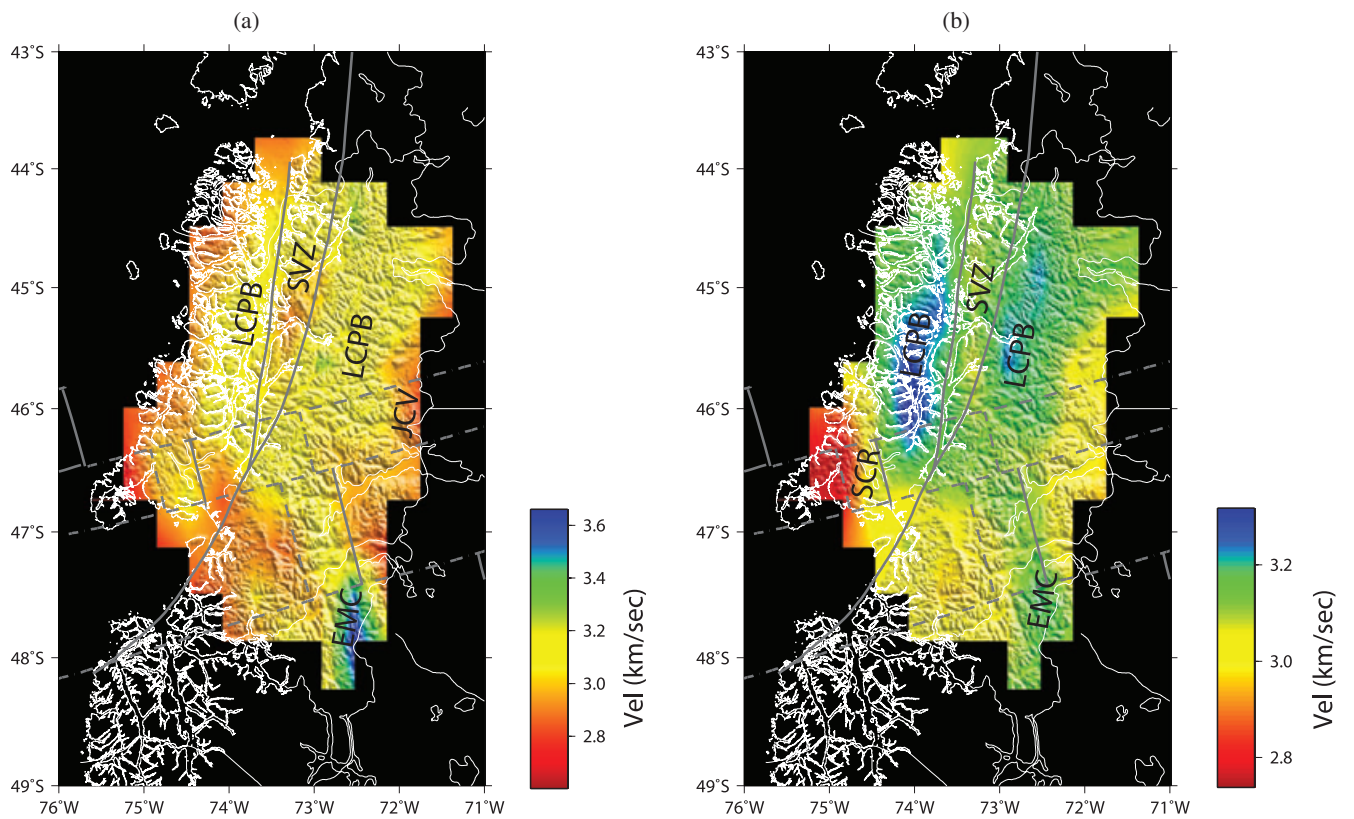
Figure 14. (a) Group velocity model for 5–10 s periods: Lower Cretaceous Patagonian Batholith (LCPB), Southern Volcanic Zone (SVZ), Jurassic-Cretaceous volcaniclastic deposits (JCV), Eastern Metamorphic Complex (EMC). (b) Group velocity model for 10–20 s periods: Lower Cretaceous Patagonian Batholith (LCPB), Southern Volcanic Zone (SVZ), Eastern Metamorphic Complex (EMC), Subducted Chile Ridge (SCR).
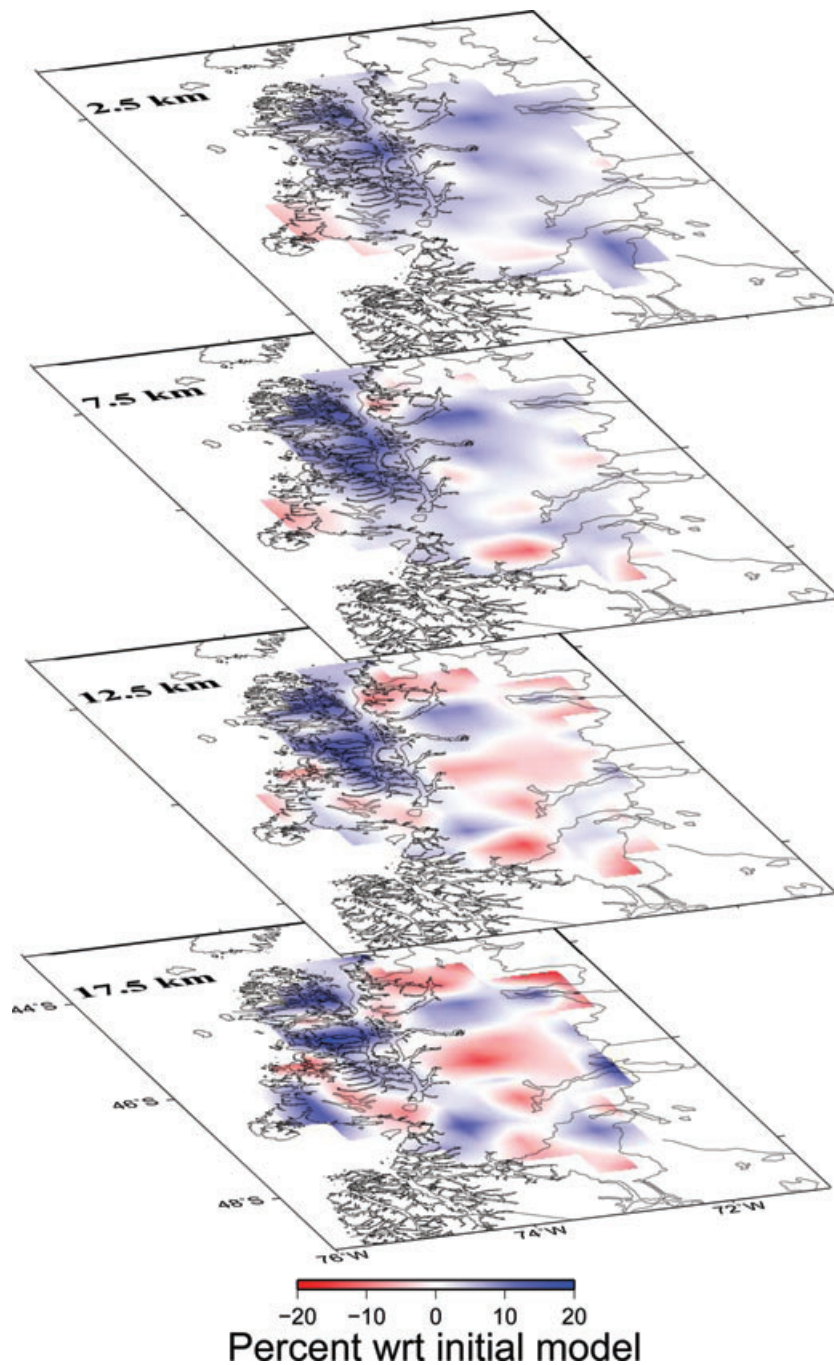
Figure 15. 3-D inversion derived from dispersion analysis; the colour bands correspond to the percentage variation with respect to the calculated 1-D model (Fig. 10).

crustal seismic velocities correlate well with known geological features. We find high crustal velocities where the North Patagonian Batholith outcrops or is likely present at depth, and relatively low velocities correlate with the active volcanic arc of the Southern Volcanic Zone and the Liquiñe-Ofqui intra-arc shear zone, the recent Chile Ridge subduction beneath the Taitao Peninsula, and a sedimentary sequence due to glacial sediment outflow into the NE Golfo de Penas. A pronounced high velocity anomaly in the southeastern portion of the study area correlates with high-elevation outcrops of highly compacted metamorphic rocks of the Paleozoic Eastern Metamorphic Complex.

REFERENCES

Bensen, G.D., Ritzwoller, M.H., Barmin, M.P., Levshin, A.L., Lin, F., Moschetti, M.P., Shapiro, N.M. & Yang, Y., 2007. Processing seismic ambient noise data to obtain reliable broad-band surface wave dispersion measurements, *Geophys. J. Int.,* **169,** 1239–1260, doi:10.1111/j.1365-246X.2007.03374.x.

Breitsprecher, K. & Thorkelson, D.J., 2009. Neogene kinematic evolution of the Nazca–Antarctic–Phoenix slab windows beneath Patagonia and the Antarctic Peninsula, *Tectonophysics,* **464,** 10–20.

Campillo, M. & Paul, A., 2003. Long-range correlations in the diffuse seismic coda, *Science,* **229,** 547–549.

Cande, S.C. & Leslie, R.B., 1986. Late Cenozoic tectonics of the southern Chile trench, *J. geophys. Res.,* **91,** 471–496.

Cande, S.C., Leslie, R.B., Parra, J.C. & Hobart, M., 1987. Interaction between the Chile Ridge and the Chile Trench: geophysical and geothermal evidence, *J. geophys. Res.,* **92,** 495–520.

Cembrano, J. & Herve, F., 1993. The Liquiñe-ofqui fault zone: a major cenozoic strike-slip duplex in the southern andes, in *Proceedings of the 2nd Int. Symp. Andean Geodynam. (ISAG),* Oxford, pp. 175–178.

Cembrano, J., Herve, F. & Lavenu, A., 1996. The Liquiñe-Ofqui fault zone: a long-lived intra-arc fault system in southern Chile, *Tectonophys.,* **259,** 55–66.

Eagles, G., Gohlb, K. & Larter, R., 2009. Animated tectonic reconstruction of the Southern Pacific and alkaline volcanism at its convergent margins since Eocene times, *Tectonophys.,* **464,** 21–29.

Escobar, F., 1980. *Mapa geológico de Chile,* escala 1:1.000.000. Servicio Nacional de Geología y Minería, Santiago, Chile.

Espinoza, F., *et al*. 2005. Petrogenesis of the Eocene and Mio-Pliocene alkaline basaltic magmatism in Meseta Chile Chico, southern Patagonia, Chile: evidence for the participation of two slab windows, *Lithos,* **82,** 315–343.

Espinoza, F., *et al*. 2008. Bi-modal back-arc alkaline magmatism after ridge subduction: Pliocene felsic rocks from central Patagonia (47°S), *Lithos,* **101,** 191–217.

Fang, Z., Boucot, A., Covacevich, V. & Herve, F., 1998. Discovery of late triassic fossils in the Chonos metamorphic complex, southern Chile, *Rev. Geol. Chile,* **25,** 165–173.

Forsythe, R.D. & Nelson, E.P., 1985. Geological manifestations of ridge collision: evidence from the Golfo de Penas-Taitao Basin, Southern Chile, *Tectonics,* **4,** 477–495.

Forsythe, R.D., Nelson, E.P., Carr, M.J., Kaeding, M.E., Herve, F., Mpodozis, C., Soffia, J.M. & Harambour, S., 1986. Pliocene near-trench magmatism in southern Chile: a possible manifestation of ridge collision, *Geology,* **14,** 23–27.

Gerstoft, P., Sabra, K.G., Roux, P., Kupferman, W.A. & Fehler, M.C., 2006. Green's functions extraction and surface-wave tomography from microseisms in southern California, *Geophysics,* **71,** S123–S131.

Gorring, M.L., Kay, S.M., Zeitler, P.K., Ramos, V.A., Rubiolo, D., Fernández, M.I. & Panza, J.L., 1997. A slab window origin for Neogene Patagonian plateau lavas (46.50 to 49.500S), *Tectonics,* **16,** 1–17.

Guivel, C., *et al*. 2006. Miocene and Lat Quaternary Patagonian basalts (46–47°S): geochronometric and geochemical evidence for slab tearing due to active spreading ridge subduction, *J. Volc. Geotherm. Res.,* **149,** 346–370.

Gutiérrez, F., Gioncada, A., González Ferran, O., Lahsen, A. & Mazzuoli, R., 2005. The Hudson Volcano and surrounding monogenetic centres (Chilean Patagonia: an example of volcanism associated with ridge-trench collision environment, *J. Volc., Geotherm. Res,* **145,** 207–233.

Herrmann, R. & Ammon, C.J., 2002. Computer programs in seismology: surface waves, in *Receiver Functions and Crustal Structure,* Vol. 3.20, St. Louis University, http://www.eas.slu.edu/People/RBHerrmann/ComputerPrograms.html .

Herve F., Calderon, M. & Faundez, V., 2008. The metamorphic complexes of the Patagonian and Fuegian Andes, *Geol. Acta,* **6,** 43–53.

Lagabrielle, Y., Le Moigne, J., Maury, R.C., Cotten, J. & Bourgois, J., 1994. Volcanic record of the subduction of an active spreading ridge, Taitao Peninsula (southern Chile), *Geology,* **22,** 515–518.

Lagabrielle, Y., Guivel, C., Maury, R.C., Bourgois, J., Fourcade, S. & Martin, H., 2000. Magmatic-tectonic effects of high thermal regime at the site of active ridge subdution: the Chile Triple Junction model, *Tectonophysics,* **326,** 255–268.

Lagabrielle, Y., Suarez, M., Rossello, E.A., Herail, G., Martinod, J., Regnier, M. & de la Cruz, R., 2004. Neogene to Quaternary tectonic evolution of the Patagonian Andes at the latitude of the Chile triple Junction, *Tectonophys.,* **385,** 211–241.

Lagabrielle, Y., *et al*., 2007. Pliocene extensional tectonics in the Eastern Central Patagonian Cordillera: geochronological constraints and new field evidence, *Terra Nova,* **19,** 413–424.

Larose, E., Derode, A., Campillo, M. & Fink, M., 2004. Imaging from one-bit correlations of wideband diffuse wave fields, *J. appl. Phys.,* **95,** 8393–8399.

Levshin, A., Ratnikova, L., Berger, J., 1992. Peculiarities of surface-wave propagation across Central Eurasia, Bulletin, *Bull. seism. Soc. Am.,* **82,** 2464–2493.

Lin, F.-C., Ritzwoller, M.H., Townend, J., Bannister, S. & Savage, M.K., 2007. Ambient noise Rayleigh wave tomography of New Zealand, *Geophys. J. Int.,* **170,** 649–666.

Lobkis, O.I. & Weaver, R.L., 2001. On the emergence of the Green's function in the correlations of a diffuse field, *J. acoust. Soc. Am.,* **110,** 3011–3017.

Murdie, R.E. & Russo, R.M., 1999. Seismic anisotropy in the region of the Chile Margin Triple Junction, *J. South Am. Earth Sci.,* **12,** 261–270.

Murdie, R.E., Prior, D.J., Styles, P., Flint, S.S., Pearce, R.G. & Agar, S.M., 1993. Seismic responses to ridge-transform subduction: Chile triple junction, *Geology,* **21,** 1095–1098.

Murdie, R.E., Styles, P., Prior, D.J. & Daniel, A.J., 2000. A new gravity map of southern Chile and its preliminary interpretation, *Rev. Geol. Chile,* **27,** 49–63.

Naranjo, J., Moreno, H. & Banks, N., 1993. La erupcion del volcan Hudson en 1991 (46s), Region XI, Aisen, Chile, *Chile Boletin,* **44,** 1–50.

Nelson, E., Forsythe, R., Diemer, J., Allen, M. & Urbina, O., 1993. Taitao Ophiolite: a ridge collision ophiolite in the forearc of southern Chile, *Rev. Geol. Chile,* **20,** 137–165.

Pankhurst, R.J., Weaver, S.D., Herve, F. & Larrondo, P., 1999. Mesozoic-Cenozoic evolution of the north Patagonian Batholith in Aysen, southern Chile, *J. Geol. Soc. Lond.,* **156,** 673–694.

Parada M.A., Lahsen, A. & Palacios, C., 2001. Ages and geochemistry of Mesozoic-Eocene back-arc volcanic rocks in the Aysen region of the Patagonian Andes, Chile, *Rev. Geol. Chile,* **28,** 25–46.

Ramos, V.A. & Kay, S.M., 1992. Southern Patagonian plateau basalts and deformation: backarc testimony of ridge collisions, *Tectonophysics,* **18,** 261–282.

Rosenau, M., Melnick, D., Echtler, H., 2006. Kinematic constraints on intra-arc shear and strain partitioning in the southern Andes between 38° and 42° S latitude, *Tectonics,* **25,** TC4013, doi:10.1029/2005TC001943.

Russo, R.M., Gallego, A., Comte, D., Mocanu, V.I., Murdie, R.E., Mora, C. & VanDecar, J.C., 2010a. Triggered seismic activity in the Liquine-Ofqui fault zone, southern Chile, *Geophys. J. Int.*, submitted.

Russo, R.M., VanDecar, J.C., Comte, D., Mocanu, V.I., Gallego, A. & Murdie, R.E., 2010b. Subduction of the Chile Ridge: upper mantle structure and flow, *GSA Today,* in press.

Shapiro, N.M. & Campillo, M., 2004. Emergence of broadband rayleigh waves from correlations of the ambient seismic noise, *Geophys. Res. Lett.,* **31,** L07614, doi:10.1029/2004GL019491.

Shapiro, N.M., Campillo, M., Stehly, L. & Ritzwoller, M.H., 2005. High-resolution surface wave tomography from ambient seismic noise, *Science,* **307,** 1615, doi:10.1126/science.1108339.

Shibuya, T., Komiya, R., Anma, R., Ota, T., Omori, S., Kon, Y., Yamamato, S. & Maruyama, S., 2007. Progressive metamorphism of the Taitao ophiolite: evidence for axial and off-axial hydrothermal alterations, *Lithos,* **98,** 233–260.

Snieder, R., 2004. Extracting the Green's function from correlation of coda waves: a derivation based on stationary phase, *Phys. Rev. E.,* **69,** 046610, doi:10.1103/PhysRevE.69.046610.

Tarantola, A., 1987. *Inverse Problem Theory and Methods for Model Parameter Estimation,* Soc. Industrial App. Math., Philadelphia.

Thompson, S. & Herve, F., 2002. New time contraints of the age of metamorphism at the ancestral Pacific Gondwana margin of southern Chile (42–52s), *Rev. Geol. Chile,* **29,** 151–165.

Wang, K., Hu, Y., Bevis, M., Kendrick, E., Vargas, R.B. & Lauria, E., 2007. Crustal motion in the zone of the 1960 Chile earthquake: detangling earthquake-cycle deformation and forearc-sliver translation, *Geochem. Geophys. Geosyst.,* **8,** Q10010, doi:10.1029/2007GC001721.